

# Numerical bifurcation study of electrohydrodynamic convection in nematic liquid crystals

S. J. Tavener\*

Department of Math, Penn State University, State College, Pennsylvania 16802  
and Department of Math, Colorado State University, Fort Collins, Colorado 80523

T. Mullin<sup>†</sup> and G. I. Blake

Department of Physics and Astronomy, University of Manchester, United Kingdom

K. A. Cliffe<sup>‡</sup>

AEA Technology, Harwell, United Kingdom

(Received 30 June 2000; published 27 December 2000)

We present the results of a numerical investigation of the Ericksen-Leslie equations for the problem of electrohydrodynamic convection in a nematic liquid crystal. The combination of a finite element approach and numerical bifurcation techniques allows us to provide details of the basic flow and include the physically relevant effect of nonslip side walls. We are also able to include material properties as parameters and this permits us to draw comparisons with available experimental data. We then compare and contrast the bifurcation structure with that of Rayleigh-Bénard and Taylor-Couette flows and explore the role of symmetries by including a fringing electric field.

DOI: 10.1103/PhysRevE.63.011708

PACS number(s): 61.30.-v, 47.20.-k, 83.80.-k

## I. INTRODUCTION

It has been well known since the paper by Helfrich [1], that when an electric field is applied across a thin layer of nematic liquid crystal, a hydrodynamic instability can occur above a critical field strength. In modern parlance, this is an example of a bifurcation and the purpose of this work is to compare and contrast its characteristics with the more familiar hydrodynamic instabilities of Rayleigh-Bénard and Taylor-Couette flows. The length and velocity scales involved in these microscopic flows are small so that the Reynolds number is very much less than one. The nonlinearity which gives rise to the instability originates in the material properties. Nematic liquid crystals differ from normal isotropic fluids since they exhibit long-range orientational ordering. They contain rodlike molecules which are arranged, on average, with their long axes parallel to one another. The direction of alignment can be described by the unit vector  $\mathbf{n}$  which is called the director. However, they flow readily since their usual viscosity is comparable with that of normal fluids. The continuum equations of motion for a nematic are the Ericksen-Leslie equations and there is considerable evidence to suggest that they provide a good model of the flow properties. The interested reader is referred to [2,3], and [4] for a discussion of the rich properties of nematic and other liquid crystals.

The basic experimental configuration is shown in Fig. 1. The first explanation of electrohydrodynamic convection by Helfrich [1] extended ideas of Carr [5] on the creation of

torques in anisotropic fluids by charge segregation. The proposed disturbance of the director field and resulting charge separation, flow, and hydrodynamic torque is described schematically in Fig. 2. It provided a satisfactory explanation for the experimental observation of roll instabilities by Williams [6] and Kasputin [7]. Helfrich's dc model was extended to time-dependent fields by Dubois-Violette *et al.*, [8] since most experiments are performed using ac fields to avoid practical problems associated with charge injection when dc voltages are applied. They found different types of instability occurring at low and at high frequencies, and called the former the conduction and the latter the dielectric regime, with a critical frequency dividing the two. The one-dimensional theories of Helfrich and Dubois-Violette *et al.* were extended to two dimensions by Penz and Ford [9] who took into account the upper and lower boundaries. A review of this early work is given by [10]. The experimental work has also been developed by [11] and [12] to include multiple patterns and spatiotemporal chaos including defects. A modern account of this research can be found in [13].

Nonlinear pattern forming instabilities in electrohydrodynamic convection have been explored in [14] and [15] using a Galerkin projection approach. In order to explore the steady-state selection mechanisms which establish the form of the primary cellular flows, we have adopted a general finite-element technique instead. This provides the added advantage of making the investigation of the effect of varying boundary conditions at both the top and bottom surfaces and the lateral walls straightforward.



FIG. 1. Schematic diagram of a cell.

\*Email address: tavener@math.colostate.edu;

http://www.math.colostate.edu/~tavener

†Email address: tom.mullin@man.ac.uk;

http://reynolds.ph.man.ac.uk/

‡Email address: andrew.cliffe@aeat.co.uk

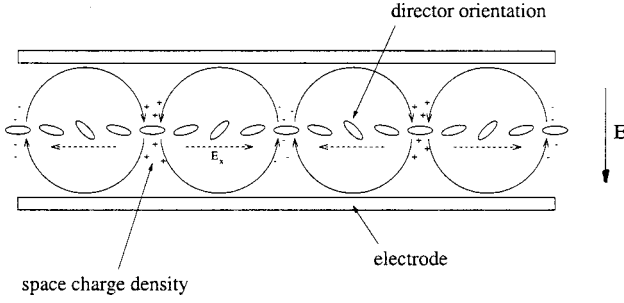


FIG. 2. Schematic diagram of the Carr-Helfrich instability mechanism.

The onset of convection can be considered as a pitchfork bifurcation, where the flow breaks the midplane symmetry and is analogous to Rayleigh-Bénard convection with a Boussinesq fluid. To date, attempts to observe both branches of the pitchfork bifurcation experimentally have failed, see [16] and [17], where the side boundary conditions are different in each case. This is unlike the situation with Rayleigh-Bénard convection where the full bifurcation structure has been observed in small aspect ratio experiments by [18] and [19], but is qualitatively the same as for Taylor-Couette flow as reviewed by [20]. One motivation of the present study was to attempt to understand this paradox. Hirata and Tako [16] have proposed a physical explanation for their observation based on the existence of free ions having only one sign and the observed localization of impurities near the walls.

Our numerical approach allows us to explore finite-size effects which are of great practical significance since many modern devices using these materials are becoming smaller and there is a need for a detailed understanding of flow properties. In addition, practical difficulties in dealing with multiplicity in the solution set in detailed scientific studies of instabilities has led to some investigators using microscopic apparatus to isolate individual dynamical events which lead to low-dimensional chaos. (See [16,21,22,23,24], and [17].) Hence there is also a need here for calculations of flows in finite domains.

We first discuss the essential details of the equations of motion and outline the numerical methods used to solve them. The detailed structure of one particular fully nonlinear convecting solution is shown to be in accord with the Carr-Helfrich model. We then discuss the role of aspect ratio and boundary conditions on the convecting solutions and show how multiple stable solutions arise via secondary bifurcation. The advantage of our numerical approach is then exploited to investigate the effect of material properties on electrohydrodynamic instabilities. Finally, we address the physically relevant situation of the effects of a fringing electric field.

## II. GOVERNING EQUATIONS AND NUMERICAL METHODS

The continuum theory of Ericksen [25] and Leslie [26] for nematic liquid crystals assumes that the average molecular axis is described locally by a unit vector  $\mathbf{n}$  and that the material is incompressible. That is, the constraints

$$n_i n_i = 1, \quad (1)$$

$$v_{i,i} = 0, \quad (2)$$

apply, where  $\mathbf{v}$  is the fluid velocity.

Balance laws representing conservation of linear and angular momentum are

$$\rho \dot{v}_i = \rho F_i + t_{ij,j}, \quad (3)$$

$$\rho M_i + e_{ijk} t_{kj} + l_{ij,j} = 0, \quad (4)$$

where  $\mathbf{F}$  and  $\mathbf{M}$  represent body forces and moments per unit mass,  $\mathbf{t}$  and  $\mathbf{l}$  are the stress and couple stress tensors, respectively, the superposed dot denotes the material time derivative and  $e_{ijk}$  is the alternating tensor. The inertial term has been omitted from the second equation, since it is generally considered negligible. The stress and couple stress tensors have the form

$$t_{ij} = -p \delta_{ij} - \frac{\partial W}{\partial n_{k,j}} n_{k,i} + \tilde{t}_{ij}, \quad (5)$$

$$l_{ij} = e_{ipq} n_p \frac{\partial W}{\partial n_{q,j}}, \quad (6)$$

where the pressure,  $p$ , arises from the constraint (2),  $W$  is the elastic energy density, and  $\tilde{\mathbf{t}}$  is the dynamic part of the stress tensor. The elastic energy density is assumed, following Frank [27], to have the form

$$2W = K(n_{i,i})^2 + K_2(n_i e_{ijk} n_{k,j})^2 + K_3 n_{i,p} n_p n_{i,q} n_q + (K_2 + K_4)[n_{i,j} n_{n,i} - (n_{i,i})^2], \quad (7)$$

where the  $K_i$  are the elastic coefficients which are constants for a given material. Following arguments proposed by Ericksen [28], the elastic constants satisfy

$$K_1 > 0, \quad K_2 > 0, \quad K_3 > 0. \quad (8)$$

These conditions are necessary in order that the conformation of the undistorted nematic corresponds to a minimum of the free energy.

The dynamic part of the stress tensor is linear in the velocity gradients and has the form

$$\tilde{t}_{ij} = \alpha_1 n_p n_k S_{pk} n_i n_j + \alpha_2 N_i n_j + \alpha_3 N_j n_i + \alpha_4 S_{ij} + \alpha_5 S_{ip} n_p n_j + \alpha_6 S_{jp} n_p n_i, \quad (9)$$

where

$$S_{ij} = \frac{1}{2}(v_{i,j} + v_{j,i}), \quad A_{ij} = \frac{1}{2}(v_{i,j} - v_{j,i}), \quad N_i = \dot{n}_i - A_{ij} n_j, \quad (10)$$

and the viscosity coefficients  $\alpha_i$  are constants. Throughout we adopt the Parodi relation [29]

$$\alpha_6 = \alpha_2 + \alpha_3 + \alpha_5. \quad (11)$$

The intrinsic viscous moment in Eq. (4) is then

$$e_{ijk}[\tilde{t}_{ij}] = e_{ijk}n_j\tilde{g}_k, \quad (12)$$

where  $[\tilde{\mathbf{t}}]$  represents the skew-symmetric part of  $\tilde{\mathbf{t}}$  and

$$\tilde{g}_i = (\alpha_2 - \alpha_3)N_i + (\alpha_5 - \alpha_6)S_{ij}n_j. \quad (13)$$

Likewise, the body moment arising from the external electric field can be written in terms of a contribution associated with  $\mathbf{n}$  and one has

$$\rho M_i = e_{ijk}n_j G_k, \quad (14)$$

$$G_i = \epsilon_0 \Delta \epsilon (E_j n_j) E_i, \quad (15)$$

$$\Delta \epsilon = \epsilon_{\parallel} - \epsilon_{\perp}, \quad (16)$$

where  $\epsilon_{\parallel}$  and  $\epsilon_{\perp}$  denote the dielectric susceptibilities of the material parallel and perpendicular to the director, respectively.

Using Eqs. (12) and (14), the angular momentum equation becomes

$$\left( \frac{\partial W}{\partial n_{i,j}} \right)_{,j} - \frac{\partial W}{\partial n_i} + G_i + \tilde{g}_i + \gamma n_i = 0, \quad (17)$$

where the scalar  $\gamma$  is a Lagrange multiplier which arises from the constraint (1). The balance of linear momentum equation becomes

$$\rho \dot{v}_i = \rho F_i - \tilde{p}_{,i} + h_i + \tilde{t}_{ij,j}, \quad (18)$$

with

$$\tilde{p} = p + W + \psi, \quad (19)$$

and

$$\tilde{h}_i = \tilde{g}_j n_{j,i}, \quad (20)$$

where  $\psi$  denotes the energy associated with the electric field. Finally, to place restrictions on the viscosity coefficients, we use the entropy inequality

$$(\tilde{t}_{ij})S_{ij} - \tilde{g}_i N_i \geq 0, \quad (21)$$

where the round brackets indicate the symmetric part of the dynamic stress tensor  $\tilde{\mathbf{t}}$ .

Equations (17) and (18) together with Eqs. (7), (9), (10), (13), and (15) are generally known as the Ericksen-Leslie equations and model flows of nematic liquid crystals that are free of ions. However, these equations are insufficient to describe electrohydrodynamic convection in nematics since ionic impurities are always present and the movement of ions in the sample comprises an essential part of the instability mechanism as described by [4]. We, therefore, supplement the Ericksen-Leslie equations with Poisson's equation and the equation for conservation of charge. These are

$$\epsilon_0 D_{i,i} = \rho_e, \quad (22)$$

$$\dot{\rho}_e + j_{i,i} = 0, \quad (23)$$

respectively, where  $\mathbf{D}$  is the electric displacement given by

$$D_i = \epsilon_{\perp} E_i + \Delta \epsilon E_j n_j n_i \quad (24)$$

(see, e.g., [30]),  $\rho_e$  is the charge density within the material and  $\mathbf{j}$  is the current density given by

$$j_i = \sigma_{\perp} E_i + \Delta \sigma E_j n_j n_i, \quad (25)$$

$$\Delta \sigma = \sigma_{\parallel} - \sigma_{\perp}, \quad (26)$$

where the nematic's conductivities parallel and perpendicular to the director are given by  $\sigma_{\parallel}$  and  $\sigma_{\perp}$ , respectively. For most nematic materials  $\Delta \sigma$  is positive. Finally,

$$e_{ijk} E_{k,j} = 0. \quad (27)$$

A recent extension of the above description for electrohydrodynamic convection has been proposed by [31] who consider two active ionic species. A bipolar electrodiffusion model may provide an explanation for the direct onset of traveling waves observed in thin samples of nematic liquid crystals with low conductivity when subject to a high-frequency ac applied field. The standard model is however believed to be appropriate for the parameter regimes considered in the present study.

Based on experimental observations of the initial instability we assume that the flow is two dimensional so that the director, velocity, and electric field vectors satisfy

$$\mathbf{n} = (\cos \theta, 0, \sin \theta), \quad \mathbf{v} = (u, 0, v), \quad \mathbf{E} = (-\phi_{,x}, 0, -\phi_{,z}), \quad (28)$$

where  $\theta$ ,  $u$ ,  $v$ , and  $\phi$  are all functions of  $x$  and  $z$ . We assume that the nematic liquid crystal is subject to an external dc electric field acting on the area  $A = [-l/2, l/2] \times [-d/2, d/2]$  with the edges of the active area being at  $x = \pm l/2$  and the plates at  $z = \pm d/2$ . Most experiments are performed using ac fields to minimize the problem of charge injection at the electrodes. Despite the fact that we consider the dc case without charge injection we obtain good agreement with experimental results. The angle  $\theta$  is a measure of the deflection of the director away from alignment with the plates and  $\phi$  is the electric potential. Notice that the expressions for  $\mathbf{n}$  and  $\mathbf{E}$  automatically satisfy the constraints (1) and (27). The modified pressure,  $\tilde{p}$ , and the charge density,  $\rho_e$ , are also assumed to be functions of  $x$  and  $z$  alone. In order to simplify the problem somewhat we neglect inertial terms (see [32]) and set  $\alpha_1 = 0$ , since  $\alpha_1$  has been found to be very small in most instances.

In order to implement the finite-element method, the governing equations and boundary conditions were recast in weak form. The resulting equations were nondimensionalized by introducing the dimensionless variables

$$\hat{x} = \frac{x}{l}, \quad \hat{z} = \frac{z}{d}, \quad \hat{u} = \frac{l}{k}u, \quad \hat{v} = \frac{l^2}{dk}v, \quad \hat{p} = \frac{l^2}{K}p, \\ \hat{\rho}_e = \frac{d^2}{\epsilon_0 \epsilon_{\perp} \phi_0} \rho_e, \quad \hat{\phi} = \frac{1}{\phi_0} \phi, \quad (29)$$

where  $k = K/\alpha_2$ , and the dimensionless parameters

$$K = \frac{K_3}{K_1}, \quad \lambda = \frac{\epsilon_0 \epsilon_{\perp} \phi_0^2}{K}, \quad r = \frac{l}{d}, \quad \mu = \frac{k \epsilon_0 \epsilon_{\perp}}{\sigma_{\perp} d^2}, \\ \epsilon = \frac{\epsilon_{\parallel}}{\epsilon_{\perp}}, \quad \sigma = \frac{\sigma_{\parallel}}{\sigma_{\perp}}, \quad (30)$$

all of which are positive apart from  $\mu$  (for flow aligning, rodlike nematics  $\alpha_2 < 0$ ). Unless stated otherwise, we will use the physical values appropriate for MBBA I [*N*-(*p*-methoxybenzylidene)-*p*-butylaniline] as listed in Appendix D of [33], namely

$$\epsilon = 0.8 \quad \text{and} \quad \sigma = 1.5 \quad (31)$$

and the viscosity coefficients,

$$\alpha_2 = -0.1, \quad \alpha_3 = -0.0011, \quad \alpha_4 = 0.0826, \quad \alpha_5 = 0.0779, \quad (32)$$

in units of  $\text{kg m}^{-1} \text{s}^{-1}$ .

For a cell with a thickness of ten of microns which is typical for many experiments,  $|\mu| \approx 10^{-3}$  and for simplicity, we set

$$\mu = 0. \quad (33)$$

No-slip velocity boundary conditions and planar anchoring of the director were applied at the top and bottom plates. The charge density  $\rho_e$  was required to be zero along the conducting plates. Both no-slip and stress-free lateral walls were considered. Homeotropic anchoring of the director was applied on the no-slip lateral walls which were assumed to be perfectly insulating. The electric potentials at the top and bottom plates were  $\pm \phi_0/2$  respectively, where  $\phi_0$  was the strength of the applied field.

The finite-element code ENTWIFE (see [34]) was used to solve the coupled equilibrium equations and boundary conditions, and to construct and solve the necessary extended systems to compute loci of singular points. Isoparametric quadrilateral elements were employed with biquadratic interpolation for the velocity components  $\hat{u}$  and  $\hat{v}$ , director angle  $\theta$ , charge density  $\hat{\rho}_e$ , and electric potential  $\hat{\phi}$ . Discontinuous linear interpolation was used for the modified pressure field  $\hat{p}$ . For all choices of boundary conditions considered here, the application of the finite-element method to the weak form of the boundary value problem resulted in a nonlinear system of equations of the form

$$\mathbf{f}(\mathbf{a}, \mathbf{b}) = \mathbf{0}, \quad \mathbf{f}: \mathbf{R}^N \times \mathbf{R}^p + \mapsto \mathbf{R}^N. \quad (34)$$

Apart from the problem involving fringing electrical field discussed in Sec. III E the boundary value problem consid-

ered here is unchanged if it is reflected about the horizontal midplane between the plates or about the vertical midplane. The discretized equations (34) are equivariant with respect to a representation of the  $Z_2 \times Z_2$  symmetry group on  $\mathbf{R}^N$ . Our treatment of the symmetries follows that described in [35] who investigated the simpler problem of Bénard convection problem in a rectangular cavity.

Nontrivial branches were found to bifurcate from the trivial, nonconvecting state with an increase in the electric potential at a symmetry-breaking bifurcation point. The ordering of the bifurcations to 1-, 2-, and 3-cell flows was determined by the aspect ratio. We will call a solution which bifurcates from the trivial solution, a ‘‘primary’’ flow. The primary one-cell flows are symmetric with respect to reflection about the diagonal of the rectangular domain. It is possible for the stability of the one-cell flows to change at symmetry-breaking bifurcation points, called secondary bifurcations points. The primary two-cell flows are symmetric with respect to reflection about the vertical midplane. Secondary bifurcation points along the two-cell primary branches at which the stability of the two-cell flows changes, are associated with breaking of this reflectional symmetry. The primary three-cell flows have a threefold translational invariance when stress-free boundary conditions are applied. Secondary bifurcations along primary three-cell branches are transcritical in nature and are associated with the breaking of this threefold invariance.

The results of two convergence studies, for stress-free and for nonslip boundary conditions at the lateral walls, are given in the Appendix.

### III. RESULTS

#### A. Stress-free lateral boundary conditions

We begin the presentation of the results by discussing details of the structure of a ‘‘typical’’ nontrivial convecting flow. The stream function and contours of the director rotation, charge density and electric potential fields are shown in Figs. 3(a)–3(d) for a primary three-cell flow at an aspect ratio of 1.5 and  $\lambda = 414.23$  or 1.44 times the critical value at this aspect ratio. The voltage is thus 1.2 times the value at which the nonconvecting solution loses stability to three-cell flows. As may be seen in the stream-function plot in Fig. 3(a), there are three cells which rotate in counterclockwise, clockwise, and counterclockwise directions from left to right, respectively. There is upward flow between the first and second cells and the return downward motion lies between the second and third cells. The directors are aligned parallel to the top and bottom plates between the cells where the fluid motion is perpendicular to the walls, as shown in Fig. 3(b). They are rotated in a counterclockwise direction in the first and third cells and clockwise in the middle cell, consistent with the direction of flow. There is an accumulation of negative charges between the first and second cells as can be seen in Fig. 3(c). These are attracted towards the positively charged upper plate. A corresponding concentration of positive charges occurs between the second and third cells which are attracted towards the lower plate. The electric potential plot shown in Fig. 3(d) reflects this accumulation of charge,

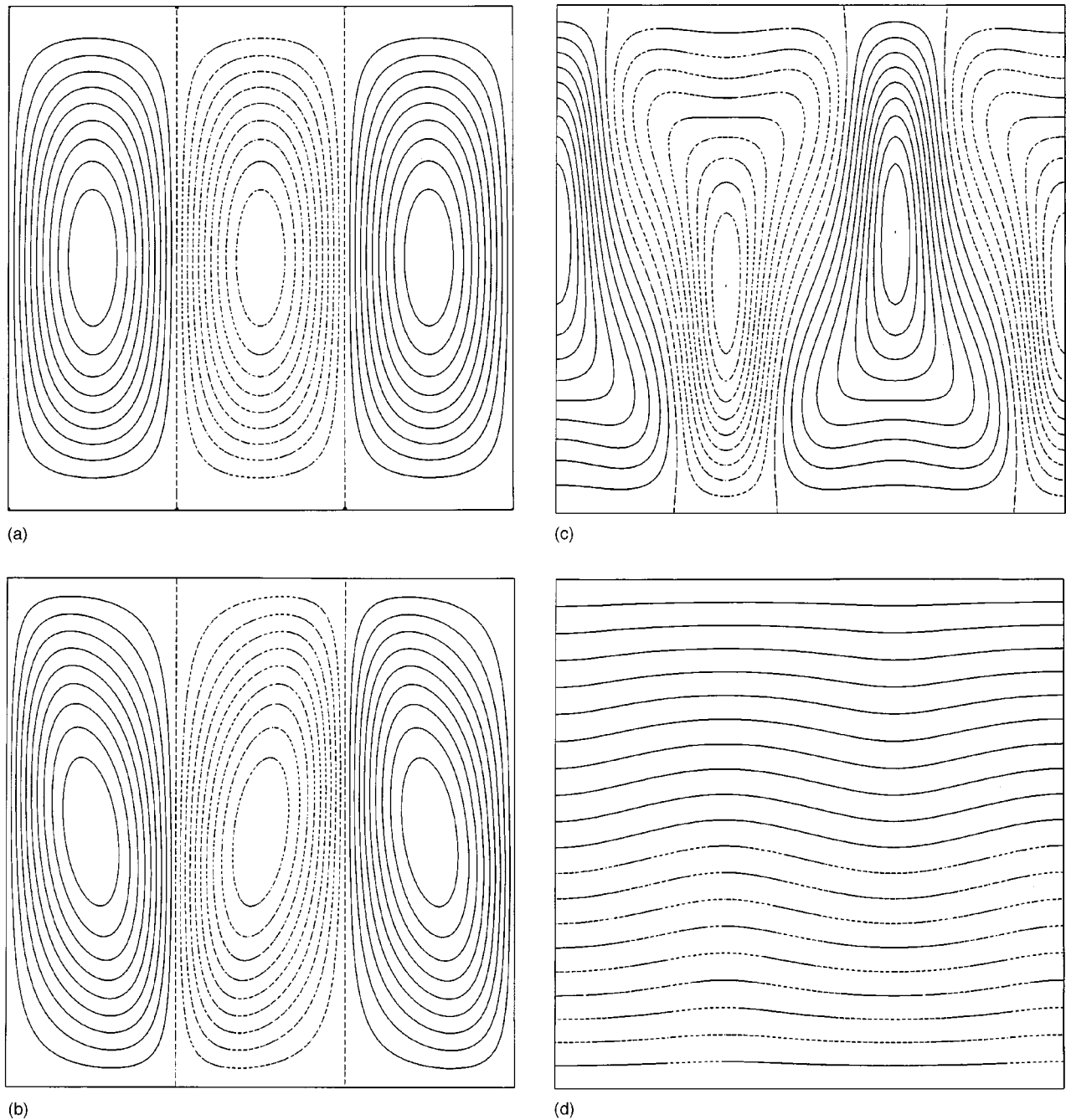


FIG. 3. Primary three-cell flow with stress-free lateral boundaries at  $\lambda=414.23$  and aspect ratio 1.5. (a) Streamlines. (b) Director angle,  $\theta$ . (c) Charge density,  $\rho$ . (d) Electric potential,  $\phi$ . Solid lines represent positive contour values, dashed lines represent negative contour values.

where the isopotential lines are seen to be deflected towards the upper plate in regions where there is accumulation of negatively charged ions and deflected towards the lower plate in regions where there is accumulation of positive charges. All of these features of the flow are consistent with the instability mechanism described by [4].

**The role of aspect ratio,  $r=l/d$**

The critical voltages at which the nonconvecting solution loses stability to one-, two-, and three-cell flows are plotted as a function of the aspect ratio  $r$  in Fig. 4. The minimum

value of the parameter  $\lambda$  at which convection occurs is  $\lambda \approx 287$  which corresponds to 5.7 volts for MBBA. This value for the critical field strength is consistent with the results of linear stability analyses performed by [9] and [33]. Henceforth we will report critical field strengths in terms of voltages, where  $\text{volts} = 0.34\sqrt{\lambda}$ .

The minimum value for the critical field strength occurs for rolls of width  $0.485d$ , i.e., approximately one-half of the distance between the plates. Defining wave number  $q$  to be the number of pairs of cells occurring in a length of  $2\pi d$  parallel to the plates,  $q_{\text{crit}} = (2\pi d)/(2 \cdot 0.485d) = 2.06\pi$ . In

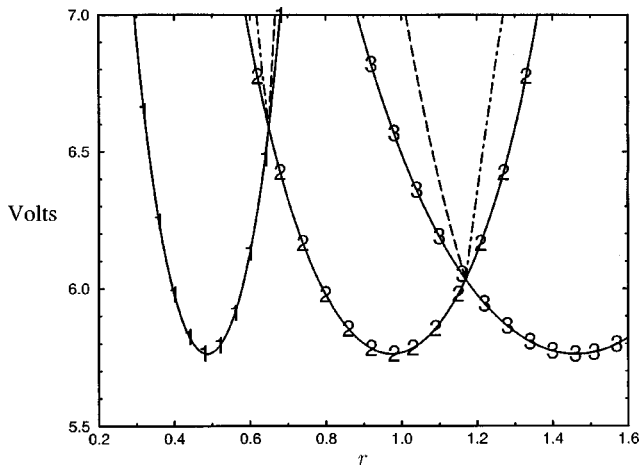


FIG. 4. Critical field strength in volts vs aspect ratio  $r$ , for bifurcation to one-, two-, and three-cell flows with stress-free lateral boundaries.

very large aspect ratio domains we, therefore, expect tall, thin rolls to be favored, a prediction that is consistent with the experimental observations of [36,37] (and with [24] and [17]), but a factor of  $1/3$  larger than that predicted by the Floquet analysis of [33] (Fig. 3, p. 1881) for the limiting dc case. Our conclusion is not consistent with the essentially circular rolls reported by [11] and predicted by the linear stability analysis of [9]. The latter work was performed for PAA (*p*-azoxyanisole) at  $125^\circ\text{C}$  which has very different values for the dielectric anisotropy, conductivity anisotropy, and elasticity ratio than those used here. Our computational studies have shown, however, that while all of these material properties affect the most unstable wavelength (see Sec. III D for a discussion of the role of the dielectric anisotropy), differences in material properties alone are insufficient to account for such a large discrepancy in the critical wavelength. Given the contradictory experimental evidence, the issue is still one for debate, but we suggest that the more sophisticated approximation of the unstable eigenvector afforded by our finite-element approach accounts for the difference with previous stability analyses. Both the linear stability analysis of [9] and the Floquet analysis of [33] assume that the  $z$  dependence of the unstable mode can be approximated by a single sinusoid, yet our finite element computations disclose a much more complex structure.

Distinct solution branches which arise at primary bifurcation points on the trivial solution can swap priority as a second parameter is changed. Secondary bifurcations mediate the smooth exchange of stability between flows with different numbers of cells as the aspect ratio is varied. The dashed line in Fig. 4 is a path of secondary, pitchfork bifurcation points on the one-cell flow branches. The chained lines are paths of secondary, pitchfork bifurcation points on the two-cell flow branches, and the dotted line indicates secondary, transcritical bifurcation on the three-cell branches. In the case of the one-cell–two-cell interaction, the exchange of stability takes place via the nine-branch mechanism discussed by [38]. At the critical value of the aspect ratio, primary and secondary bifurcation points all converge and a

smooth exchange of priority and stability of the two primary branches is mediated. The exchange process is modified slightly in the case of the two-cell–three-cell interaction, since the secondary bifurcations on the three-cell flows are transcritical in nature.

The secondary bifurcations described here restabilize unstable flows allowing multiple stable solutions to exist. This multiplicity of solutions is important as they play a major role in low-dimensional dynamics as discussed by [39].

### B. Nonslip lateral boundary conditions

Imposing nonslip rather than stress-free lateral boundary conditions has a quantitative effect not only on the critical field strength but on the convecting state that arises once this critical voltage is exceeded. The symmetries of the problem remain unchanged and convecting flows arise from the trivial, conducting solution at pitchfork bifurcation points as in the stress-free case. Considerations of symmetries alone would lead one to expect electrohydrodynamic convection in finite regions to behave similarly to confined Rayleigh-Bénard convection. This is at odds with experiments in which flows corresponding to only one branch of the pitchfork bifurcation have been observed, and is the subject of the current investigation.

Contours of the director angle and the charge density for a one-cell flow with nonslip lateral walls at an aspect ratio of 0.5 and  $\lambda=1060$  (1.21 times the critical value) are shown in Figs. 5(a) and 5(b). For comparison the director angle and charge density for a one-cell flow with stress-free lateral boundaries at an aspect ratio of 0.5 and  $\lambda=348.1$  (1.21 times the critical value) are shown in Figs. 5(c) and 5(d). The overall features of the flow are consistent with the Helfrich mechanism, as in the stress-free case, but there are significant differences between the two situations. The effect of the lateral walls on the streamlines is not very dramatic and they are not shown. The streamlines are simply more elliptical with the major axis of the ellipse aligned with the end walls. This reorientation of the flow field is also manifest on comparing the contours of director angle shown in Figs. 5(a) and 5(c). There are now regions adjacent to the end walls where the director is rotated in the opposite sense to the principal orientation. Surprisingly, however, the maximum positive rotation of the directors is approximately the same in the two cases. (Recall that both flows are shown for  $\lambda$  approximately 1.21 times the critical value.) The regions of weaker negative and positive charge densities near the left-hand and right-hand walls shown in Fig. 5(b) are also something of a surprise. These border the closed regions of charge in the interior of the flow which are not present in the stress-free case shown in Fig. 3.3(d). The maximum and minimum charge densities in Fig. 5(b) have amplitudes nearly twice those in Fig. 5(d). Close comparison of the electric potential reveals the influence of the different charge density distributions in the two cases, but the differences are minor and are again not shown.

### Role of aspect ratio, $r=l/d$

We present the results of calculations of the neutral stability curves in the aspect ratio, voltage plane for the onset of

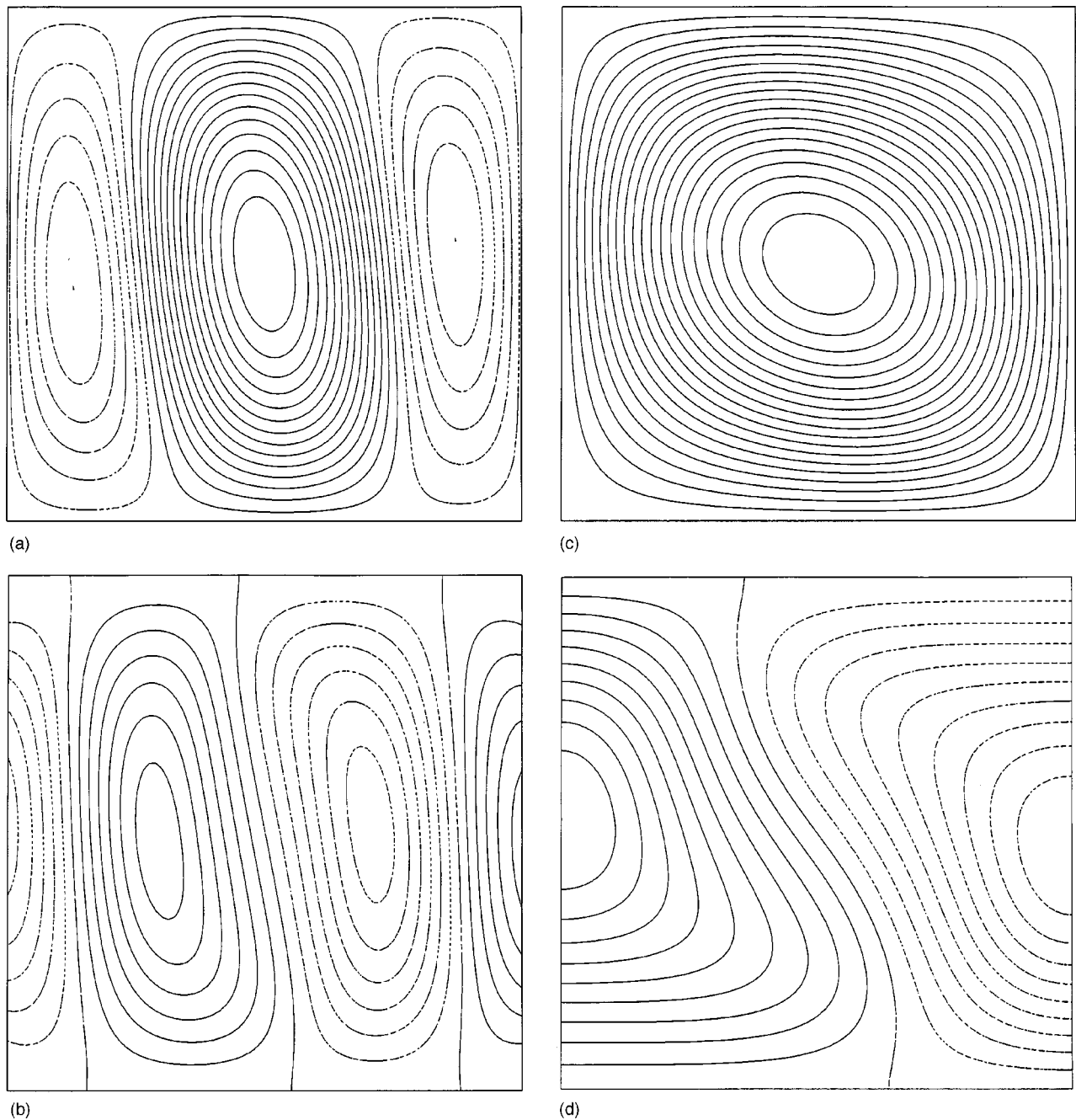


FIG. 5. Primary one-cell flow with nonslip lateral boundaries at  $\lambda=1060$  at aspect ratio 0.5. (a) Director angle,  $\theta$ . (b) Charge density,  $\rho$ . Primary one-cell flow with stress-free lateral boundaries at  $\lambda=348.1$  at aspect ratio 0.5. (c) Director angle,  $\theta$ . (d) Charge density,  $\rho$ . Solid lines represent positive contour values, dashed lines represent negative contour values.

one to five convection cells in Fig. 6. The solid lines designate loci of parameter values where stable convecting solutions bifurcate from the no flow state and the dashed curves indicate paths of the origin of unstable solutions. The numbers below the curves denote the particular state which bifurcates first in the given aspect ratio range.

Cliffe and Winters [35] investigated two-dimensional Rayleigh-Bénard flow in small aspect ratio containers and considered it as a two parameter problem with  $Z_2 \times Z_2$  symmetry. They showed that the double zero eigenvalue corresponding to the intersection of two bifurcations which break

the same  $Z_2$  symmetry, is not stable with respect to small perturbations. This was found to be true even when the perturbations respect the  $Z_2$  symmetry. The bifurcations to 1-cell and 3-cell flows (and indeed to all odd-numbered flows), break the same symmetries and hence the double singular point at which these two neutral stability curves intersect becomes disconnected. We only show the smaller of the two critical field strengths for the bifurcation to either 1- or 3-cell flows. The disconnected upper parts of the neutral stability curves are not shown for the sake of clarity. Similarly, bifurcations to 2- and 4-cell flows (and indeed to all even-

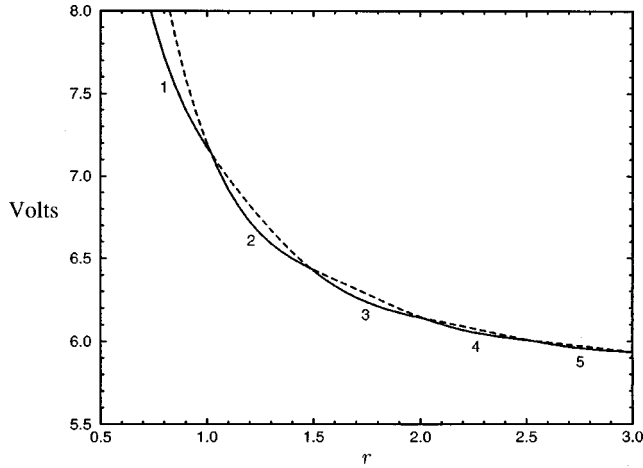


FIG. 6. Critical field strength in volts vs aspect ratio  $r$ , for cellular flows with nonslip lateral boundaries.

numbered flows) involve the breaking of the same  $Z_2$  symmetry and the double singular point at which their two neutral stability curves intersect is also not stable. Once again, only the lower part of the neutral stability curve for even-cell flows is shown in Fig. 6. Secondary bifurcations will again exist along the primary two-cell branches but these are not shown.

### C. Continuation studies with stress-free lateral walls

A significant advantage of the numerical approach we have developed is that it allows us to include material properties as parameters in the equations and to follow paths of critical points as a function of these parameters.

#### 1. The role of conductivity anisotropy, $\sigma = \sigma_{\parallel} / \sigma_{\perp}$

We show in Fig. 7 the effect of varying the conductivity anisotropy on the critical voltage for bifurcation to one-cell flows at an aspect ratio of 0.5. These critical values were

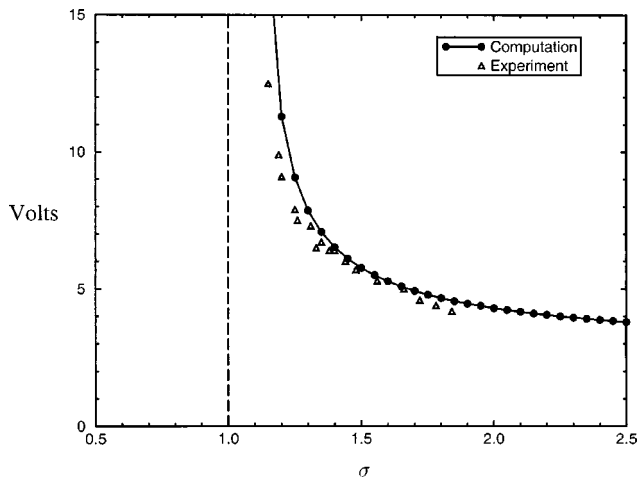


FIG. 7. Critical field strength in volts vs conductivity anisotropy  $\sigma$ , for bifurcation to one-cell flows with stress-free lateral boundaries at aspect ratio  $r=0.5$ . Triangles indicate the experimentally determined values from [40].

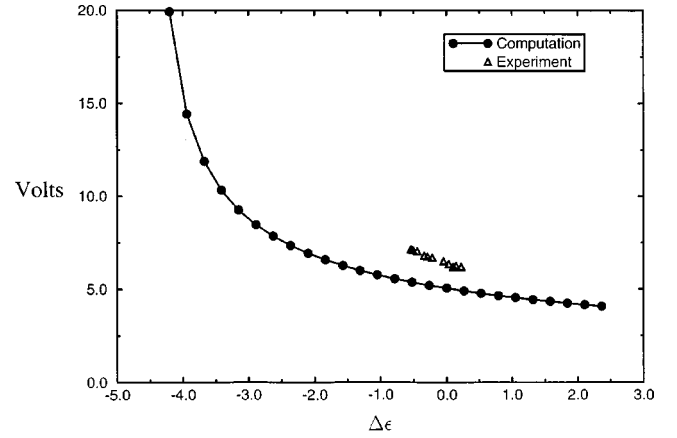


FIG. 8. Critical field strength in volts vs dielectric anisotropy  $\Delta\epsilon$ , for bifurcation to one-cell flows with stress-free lateral boundaries at aspect ratio  $r=0.5$ . Triangles indicate the experimentally determined values from [40].

computed using a  $32 \times 32$  element grid on one-quarter of the domain. The effect of  $\sigma$  on the critical voltage has previously been investigated by Barnik *et al.* [40] who obtained good agreement between experimental data and results from two-dimensional models. It is to be expected that the locus of critical voltage is asymptotic to the line  $\sigma=1$ , since that this point  $\sigma_{\parallel}=\sigma_{\perp}$ , and the charge separation required for the Carr-Helfrich instability mechanism cannot occur. Despite the fact that our results were calculated for MBBA I and dc fields, rather than the doped MBBA mixtures and ac fields used by [40], we obtained good quantitative agreement with the experimental results.

#### 2. The role of dielectric anisotropy, $\Delta\epsilon = \epsilon_{\parallel} - \epsilon_{\perp} = 1 - \epsilon$

We show in Fig. 8 the effect of varying the dielectric anisotropy on the critical voltage for bifurcation to one-cell flows at an aspect ratio of 0.5. These critical values were again computed using a  $32 \times 32$  element grid on one-quarter of the domain. The dielectric anisotropy is evidently a stabilizing factor for  $\Delta\epsilon < 0$ , since the critical voltage increases as the anisotropy decreases, i.e., as  $\epsilon_{\parallel}$  and  $\epsilon_{\perp}$  become increasingly dissimilar. These results are largely in agreement with those of [40] who investigated the parameter range on either side of  $\Delta\epsilon=0$ . Interestingly our curve is approximately the same distance below the experimental points as the theoretical work of Barnik when the dielectric anisotropy is zero, despite the differences in material properties ( $\sigma=1.3$ , cf.  $\sigma=1.5$  and  $K=1.22$ , cf.  $K=1$ ). However, unlike [40], the slope of our numerical results is approximately the same as the experiments. As we will show in Sec. III D, the most unstable wavelength changes with the dielectric anisotropy and we suspect that the difference between the two sets of calculations originates in our choice of seeking the critical field for a particular wavelength, as opposed to finding the absolute minimum of the instability curves.

Note that for  $\Delta\epsilon > 0$  we are still able to compute a critical applied field at which an instability to a convective motion arises. This is surprising, since for  $\Delta\epsilon > 0$  one would expect a static realignment of the molecules through a Fredericksz

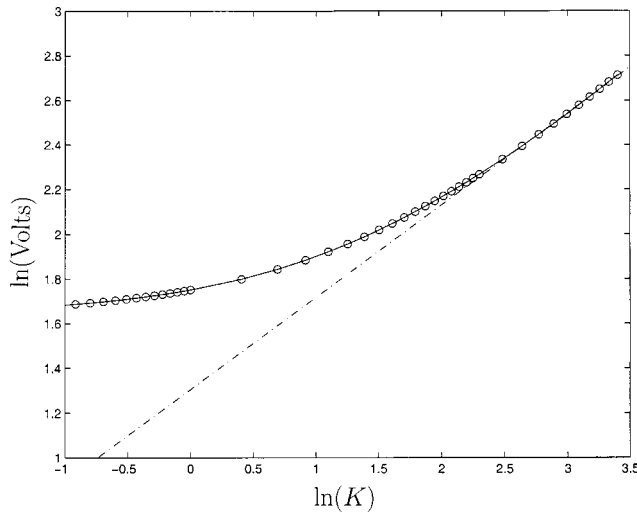


FIG. 9. The natural logarithm of the critical voltage,  $\ln(\text{Volts})$  vs the natural logarithm of the ratio of elastic constants,  $\ln(K)$ . The chained line is the least-squares best fit to the 10 largest values of  $K$  and has a slope of 0.41.

transition as discussed by [41]. The exchange between these two types of instability for  $\Delta\epsilon > 0$  will also be addressed in Sec. III D.

### 3. The role of elasticity ratio, $K=K_3/K_1$

In Fig. 9 we have plotted the natural logarithm of the critical voltage for bifurcation to one-cell flows at an aspect ratio of 0.5 against the natural logarithm of the elasticity ratio. It is clear that there is no simple relationship valid for all values of  $K$ , but for  $K > 2$ , the slope of the curve is approximately equal to  $1/2$ , indicating the square root relation predicted by [4] (p. 238). Their result, which is based on a balance of elastic, hydrodynamic and elastic torques, is expected to be valid in the limit of large  $K$  as it ignores any elastic effects due to splay.

### D. The Freedericksz transition

We now focus on the influence of the dielectric anisotropy on the wavelength of the most unstable mode. The critical voltage for the onset of one-cell flows is plotted as a function of aspect ratio in Fig. 10 for a range of dielectric anisotropies. The dashed horizontal lines indicate the theoretical value of the critical voltage for the Freedericksz transition for  $\epsilon=1.05, 1.1, 1.2, 1.3,$  and  $1.4$ . (The critical value is  $\lambda = \pi^2/\epsilon$  — see [4], p. 135). Notice that for  $0.9 \leq \epsilon \leq 1.05$  there is a distinct minimum in the neutral stability curves for the onset of electrohydrodynamic convection, suggesting that there is a favored wavelength in large aspect ratio experiments. These minima are plotted in Fig. 11, where, consistent with the results presented in Fig. 8, the critical voltage decreases as  $\epsilon$  increases. The widths of a single cell  $w$ , corresponding to these minima, are plotted in Fig. 12, where it can be seen that the most unstable wavelength increases dramatically (and in fact doubles) as  $\epsilon$  increases from 0.6 to 1.05.

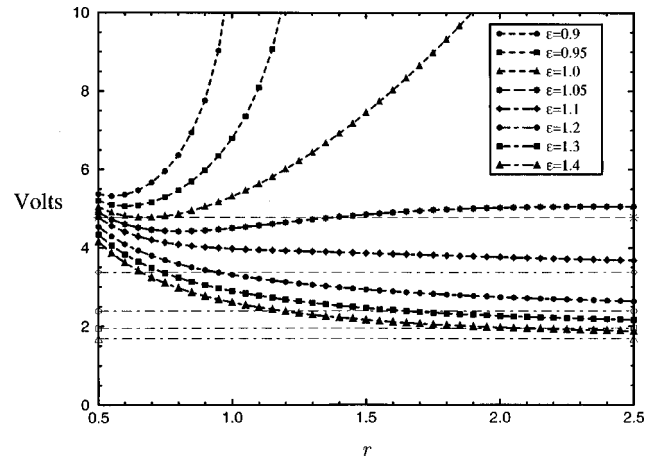


FIG. 10. Critical field strength in volts vs aspect ratio  $r$ , for one-cell flows with stress-free lateral boundaries and  $\epsilon=0.9, 0.95, 1.0, 1.05, 1.1, 1.2, 1.3, 1.4$ . Horizontal lines indicate the critical field strength for a Freedericksz transition.

For  $\epsilon=1.05$  the minimum critical field for the onset of electrohydrodynamic convection occurs below the critical field strength at which a Freedericksz transition would occur and is, therefore, the preferred instability. Consistent with [40], the results presented in Fig. 10 suggest that the transition between instability resulting in convection and the static Freedericks transition is a continuous one and that it occurs between  $1.05 < \epsilon < 1.1$ . For  $\epsilon \geq 1.1$  the loci of critical voltages for electrohydrodynamic convection have no obvious minima and approach (from above) the critical voltage for the Freedericks transition as the aspect ratio increases. The Freedericksz transition is therefore the preferred instability. We observed numerically that as the critical field strength for a convective instability approaches the value for a static Freedericks instability, the magnitudes of the  $u$  and  $v$  components of the unstable eigenvector (i.e., the strength of the convective motion) decay, further suggesting a continuum of behavior.

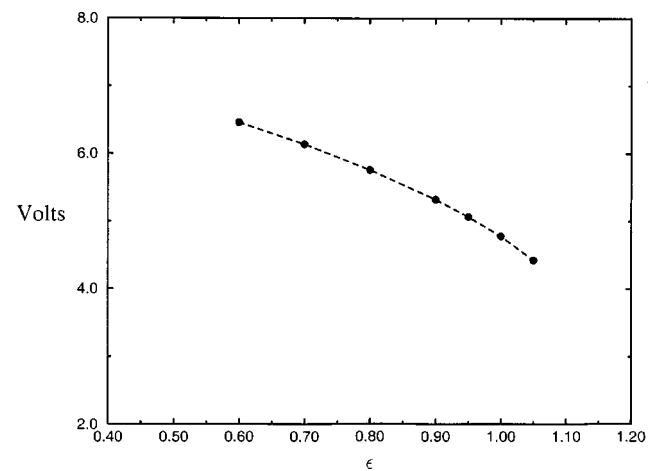


FIG. 11. Minimum critical field strength in volts vs dielectric anisotropy  $\epsilon$ , with stress-free lateral boundaries.

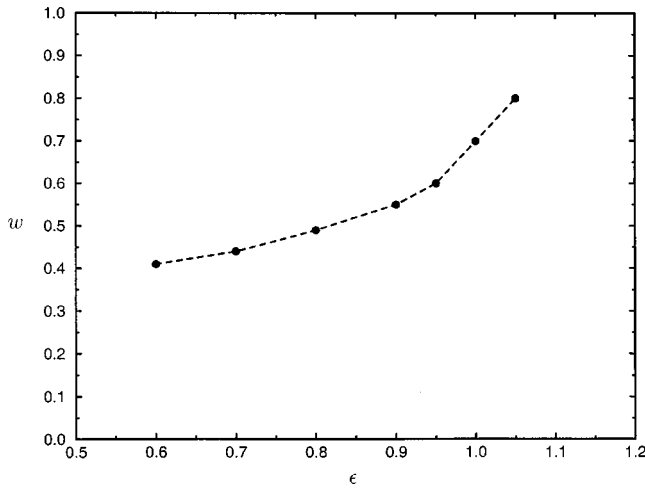


FIG. 12. Nondimensional width of a single cell  $w$  vs dielectric anisotropy  $\epsilon$ , with stress-free lateral boundaries.

**E. The effect of a fringing field**

The precise nature of the fringing electric field in a nematic near the edge of an electrode is still a topic of ongoing research—see, for example, [42] and [43]. These authors suggest that the fringing field may extend for 1 or 2 gap widths beyond the edge of the electrode. Figure 13 shows a six-cell flow viewed from above with up-welling at the left- and right-hand boundaries. The white lines indicate the edges of the two electrodes used to create an ac electric field. The lower electrode extends from left to right in Fig. 13, the upper electrode extends from top to bottom of the figure. The size of the active region is approximately  $200 \times 200 \times 50 \mu\text{m}$ . The surfaces of the electrodes have been prepared so as to anchor the directors in the horizontal direction. For this moderate voltage, the convection is clearly confined to the region in which the electrodes overlap. Our approach was to replace the upper electrode with a nonslip boundary for which only the central region was a conductor and the two outer portions were insulators, as shown schematically in Fig. 14. Only the symmetry about the vertical midplane remains, so that flows with an even number of cells do not arise via a symmetry-

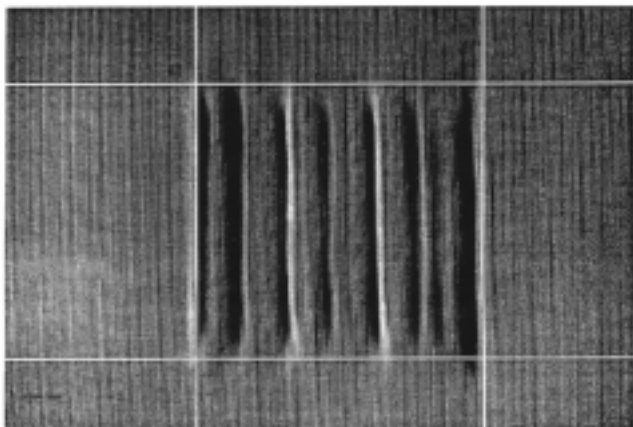


FIG. 13. Experimental realization of a six-cell flow.

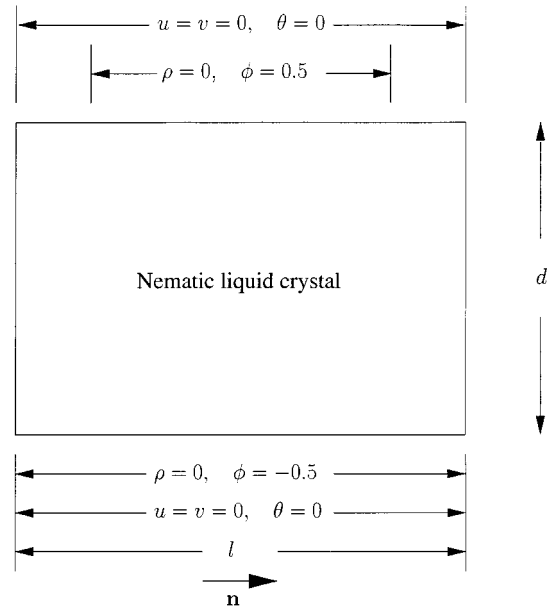


FIG. 14. Model problem to capture the effect of a fringing electric field at the lateral boundaries.

breaking bifurcation. One of the two possible two-cell flows will arise with gradual increase of the electric field, while the other will occur as a disconnected secondary flow. Figure 15 is a bifurcation diagram for the case when 90% of the upper boundary is conducting. We have chosen the vertical velocity at the point  $(\hat{x}, \hat{z}) = (-3/8, -1/4)$ , normalized so that positive velocities are upwards, i.e.,  $-\hat{v}(-3/8, -1/4)$  as a measure of the flow. The amount of disconnection is small and both types of even-cell flows would be expected to be observed in an experiment. We suggest that there must be another mechanism to account for the experimental observation.

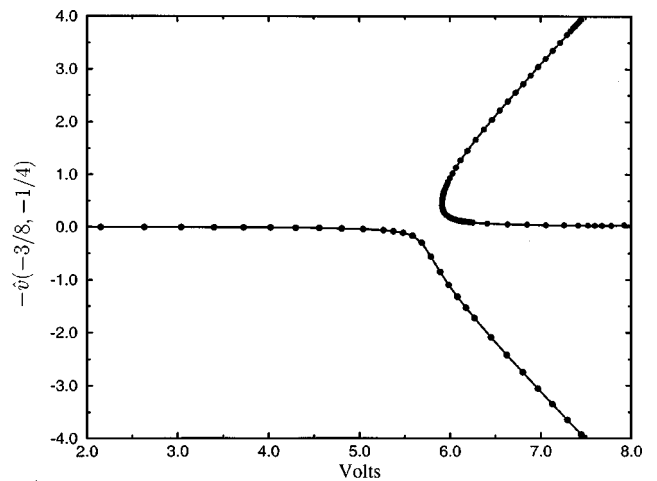


FIG. 15. Bifurcation diagram for the onset of two-cell flows at an aspect ratio of 1.0 when modeling the fringing electric field. The vertical velocity at the non-dimensionalized location  $(\hat{x}, \hat{z}) = (-3/8, -1/4)$ , normalized so that positive velocities are upwards, i.e.,  $-\hat{v}(-3/8, -1/4)$  is plotted as a function of the applied voltage.

TABLE I. Convergence study for stress-free lateral side walls.

$N$	$\lambda_N$	$(\Delta\lambda)_N$	$(\Delta\lambda)_{N/2}/(\Delta\lambda)_N$
2	292.052 96		
4	288.091 77	3.961 19	
8	287.659 44	0.432 33	9.16
16	287.622 30	0.037 14	11.64
32	287.619 70	0.002 60	14.28
64	287.619 53	0.000 17	15.29

IV. CONCLUSIONS

We have successfully carried out a numerical study of the full Ericksen-Leslie equations for electrohydrodynamic convection. Our approach has enabled us to investigate the effects of finite geometries and varying material properties and the latter has shown good quantitative agreement with available experimental data. Hence we are able to conclude that our results are relevant to the more common experimental situation where ac fields are used.

A primary goal of our work was to relate the steady bifurcation structure in this problem to those of Rayleigh-Bénard flow, which it resembles most closely mathematically and Taylor-Couette flow, which it recalls experimentally. We have been partially successful in this with the exception of elucidating the observed apparently large disconnection of the first bifurcation in experiments. Inclusion of a fringing field is insufficient to produce the desired effect. We, therefore, speculate that introducing the flexoelectric effect into the problem as suggested by [44] may be the way forward. This will change the symmetry properties and the disconnection of the resulting transcritical bifurcation by a fringing field, may be sufficient to explain the observed properties. This is the subject of future research.

ACKNOWLEDGMENTS

G.I.B. and T.M. would like to thank the Leverhulme Trust for financial support. T.M. was supported by the Shapiro Fund from the Department of Mathematics of Pennsylvania State University. S.J.T. would like to thank the National Sci-

TABLE II. Convergence study for nonslip lateral side walls.

$N$	$\lambda_N$	$(\Delta\lambda)_N$	$(\Delta\lambda)_{N/2}/(\Delta\lambda)_N$
4	880.415 35		
8	876.317 25	4.098 10	
16	875.996 45	0.320 80	12.77
32	875.971 61	0.024 84	12.91
64	875.969 88	0.001 73	14.36

ence Foundation for supporting this work under Grant No. DMS97-04714.

APPENDIX: CONVERGENCE STUDIES

1. Stress-free lateral boundary conditions

In Table I we tabulate the critical parameter  $\lambda$  corresponding to the onset of one-cell flows for an aspect ratios of  $r = 0.5$ . The top and bottom boundaries were conducting plates and stress-free conditions were applied at the lateral side walls. The computations were performed using  $N \times N$  element uniform grids on one-quarter of the domain. Let  $h$  be the characteristic size of the elements. A superconvergent  $h^4$  asymptotic convergence rate is indicated, since it appears that

$$\lim_{N \rightarrow \infty} \frac{(\Delta\lambda)_{N/2}}{(\Delta\lambda)_N} = 16,$$

where  $(\Delta\lambda)_N = \lambda_{N/2} - \lambda_N$ .

2. Nonslip lateral boundary conditions

Table II shows the critical parameter  $\lambda$  for the bifurcation from the nonconvecting state to the primary one-cell flows given conducting top and bottom plates and nonslip lateral side walls at an aspect ratio  $r = 0.5$ .

As expected due to the presence of nonslip lateral walls, the critical value of the applied electric field required to establish convective motion is considerably larger than for the case of stress-free lateral boundary conditions at equal values of the parameters. The asymptotic convergence rate for the critical parameter value appears again to be  $h^4$ .

---

[1] W. Helfrich, *J. Chem. Phys.* **51**, 4092 (1969).  
 [2] L. Blinov, *Electro-optical and Magneto-optical Properties of Liquid Crystals* (Wiley, New York, 1983).  
 [3] S. Chandrasekhar, *Liquid Crystals* (Cambridge University Press, Cambridge 1977).  
 [4] P. G. de Gennes and J. Prost, *The Physics of Liquid Crystals* (Oxford University Press, Oxford, 1993).  
 [5] E. F. Carr, *J. Chem. Phys.* **39**, 1979 (1963).  
 [6] R. Williams, *J. Chem. Phys.* **39**, 384 (1963).  
 [7] A. P. Kasputin and L. S. Larionova, *Kristallografiya* **9**, 372 (1964) [*Sov. Phys. Crystallogr.* **9**, 297 (1964)].  
 [8] E. Dubois-Violette, P. G. de Gennes, and O. Parodi, *J. Phys.* (Paris) **32**, 305 (1971).  
 [9] P. A. Penz and G. W. Ford, *Phys. Rev. A* **6**, 414 (1972).  
 [10] W. Goossens, *Adv. Liq. Cryst.* **3**, 1 (1978).  
 [11] A. Joets and R. Ribotta, *J. Phys.* (Paris) **47**, 595 (1986).  
 [12] I. Rehberg, S. Rasenat, and V. Steinberg, *Phys. Rev. Lett.* **62**, 756 (1989).  
 [13] A. Buka and L. Kramer, *Pattern Formation in Liquid Crystals* (Springer, Berlin, 1996).  
 [14] E. Plaut, W. Decker, A. Rossberg, L. Kramer, and W. Pesch, *Phys. Rev. Lett.* **79**, 2367 (1997).  
 [15] W. Pesch and U. Behn, in *Evolution of Spontaneous Structures in Dissipative Continuous Systems*, edited by F. H. Busse and

- S. C. Mueller (Springer, Berlin, 1998), pp. 335–383.
- [16] S. Hirata and T. Tako, *Jpn. J. Appl. Phys., Part 2* **21**, L607 (1982).
- [17] T. Peacock, D. Binks, and T. Mullin, *Phys. Rev. Lett.* **82**, 1446 (1999).
- [18] P. A. Warkentkin, H. J. Haucke, P. Lucas, and J. Wheatley, *Proc. Natl. Acad. Sci. U.S.A.* **77**, 6983 (1980).
- [19] M. P. Arroyo and J. M. Saviro, *J. Fluid Mech.* **235**, 325 (1992).
- [20] T. Mullin, *IMA J. Appl. Math.* **46**, 109 (1991).
- [21] S. Kai and K. Hirakawa, *Prog. Theor. Phys. Suppl.* **64**, 212 (1978).
- [22] S. Kai and W. Zimmermann, *Prog. Theor. Phys. Suppl.* **99**, 458 (1989).
- [23] D. J. Binks and T. Mullin, *Proc. R. Soc. London, Ser. A* **453**, 2109 (1997).
- [24] Y. Hidaka, K. Shimokawa, H. O. T. Nagaya, and Y. Ishibashi, *J. Phys. Soc. Jpn.* **63**, 1698 (1994).
- [25] J. L. Ericksen, *Arch. Ration. Mech. Anal.* **9**, 371 (1962).
- [26] F. M. Leslie, *Continuum Mech. Thermodyn.* **4**, 167 (1992).
- [27] F. C. Frank, *Discuss. Faraday Soc.* **25**, 19 (1958).
- [28] J. L. Ericksen, *Phys. Fluids* **9**, 1205 (1966).
- [29] O. Parodi, *J. Phys. (France)* **31**, 581 (1970).
- [30] M. Kaiser and W. Pesch, *Phys. Rev. E* **48**, 4510 (1993).
- [31] M. Treiber and L. Kramer, *Mol. Cryst. Liq. Cryst.* **261**, 311 (1995).
- [32] D. W. Berreman, *J. Appl. Phys.* **46**, 3746 (1975).
- [33] E. Bodenschatz, W. Zimmermann, and L. Kramer, *J. Phys. (France)* **453**, 1875 (1988).
- [34] K. A. Cliffe, AEAT-0823 (1996).
- [35] K. A. Cliffe and K. H. Winters, *J. Comput. Phys.* **67**, 310 (1986).
- [36] D. Meyerhofer and A. Sussman, *Appl. Phys. Lett.* **20**, 337 (1972).
- [37] P. A. Penz, *Phys. Rev. Lett.* **24**, 1405 (1970).
- [38] L. Bauer, H. Keller, and E. Reiss, *SIAM (Soc. Ind. Appl. Math.) J. Appl. Math.* **17**, 101 (1975).
- [39] T. Mullin, *The Nature of Chaos* (Clarendon, Oxford, 1995).
- [40] M. Barnik, L. Blinov, M. Grebenkin, S. Pikin, and V. Chigrinov, *Phys. Lett.* **51A**, 175 (1975).
- [41] G. I. Blake, S. Tavener, and T. Mullin, in *Dynamics and Stability of Systems* (1999), Vol. 14, p. 299.
- [42] W. J. Cassarly and S. J. Young, *Mol. Cryst. Liq. Cryst.* **210**, 1 (1992).
- [43] G. M. Storrow, H. F. Gleeson, and A. J. Murray, *Pure Appl. Opt.* **7**, 1411 (1998).
- [44] L. Kramer and W. Pesch, *Annu. Rev. Fluid Mech.* **27**, 515 (1995).